Microscopic modeling of the dielectric properties of silicon nitride

T. Anh Pham,[1] Tianshu Li,[1,2] Sadasivan Shankar,[3] Francois Gygi,[4,5] and Giulia Galli[1,6]
[1]*Department of Chemistry, University of California, Davis, California 95616, USA*
[2]*Department of Civil and Environmental Engineering, The George Washington University, Washington, DC 20052, USA*
[3]*Intel Corporation, Santa Clara, California, USA*
[4]*Department of Applied Science, University of California, Davis, California 95616, USA*
[5]*Department of Computer Science, University of California, Davis, California 95616, USA*
[6]*Department of Physics, University of California, Davis, California 95616, USA*
(Received 4 December 2010; revised manuscript received 31 March 2011; published 11 July 2011)

We investigate the differences between the dielectric properties of bulk silicon nitride and thin films, in both crystalline and amorphous structures. We show that to correctly account for the decrease of the optical (ϵ_∞) and static (ϵ_0) dielectric constants at the nanoscale, it is necessary to take into account their spatial variations within the film and at the surface. A model based on the assumption of abrupt interfaces between vacuum and the film surfaces predicts the wrong trend of the dielectric properties as a function of the film thickness, i.e., an increase of ϵ_∞ and ϵ_0 as the dimension of the film decreases. We also show that a first-principles description of the structural properties of amorphous bulk and thin films is necessary, in order to obtain structural properties in agreement with experiment, and thus electronic and dielectric properties consistent with available measurements.

DOI: 10.1103/PhysRevB.84.045308 PACS number(s): 77.84.−s, 71.15.Mb, 61.43.Dq, 63.20.dk

I. INTRODUCTION

The mechanical and electronic properties of silicon nitride (Si_3N_4) have been exploited in several technological applications. For example, because of its strength and hardness, high decomposition temperature, and good resistance to corrosion and wear, Si_3N_4 is used in heat exchangers, turbine and automotive engine components, and to fabricate cutting tools.[1,2] Plasma-enhanced chemical-vapor-deposited Si_3N_4 films are used to passivate Si solar cells.[3,4] Silicon nitride is also widely employed in the semiconductor industry for surface passivation, protection to prevent oxidation and damage, and as a mask for local oxidation.[5–7]

In addition to these applications, Si_3N_4 is receiving attention as a possible candidate material to either replace or be alloyed with SiO_2 and be part of high-κ stack of dielectric films, which are used to prevent leakage currents in modern CMOS transistors. Indeed Si_3N_4 has a higher dielectric constant than that of SiO_2 and thus it may be a good candidate to prevent or reduce tunneling-induced currents.[8–11] Furthermore, compared to SiO_2, Si_3N_4 is more stable in strong electric fields and at high temperature, and it is more effective in providing diffusion barriers to impurities such as boron.[9–11] It is therefore of interest to investigate how the dielectric properties of Si_3N_4 change at the nanoscale, as the thickness of high-κ dielectrics in devices is constantly shrinking and already of the order of a few tens of nanometers.

Here we report a theoretical study of the variation of the dielectric properties of Si_3N_4 when reducing the material dimensions from bulk to thin films, and we study both crystalline and amorphous systems. While the structural and the electronic properties of bulk crystalline Si_3N_4 have been extensively studied,[12–15] our knowledge of the structural and electronic properties of amorphous Si_3N_4 is rather limited since data on thin films with good material characterization are not widely available, and theoretical modeling for polycrystalline and amorphous structures are computationally very demanding. Theoretically, the structure of amorphous Si_3N_4 has been studied using classical potentials[16–19] and density functional theory (DFT);[20–23] however several open questions remain. For example, the effect of the size of amorphous samples generated by computer simulations, on the calculated electronic and dielectric properties, has not yet been investigated. Therefore in this paper we have first analyzed in detail the structural and dielectric properties of bulk a-Si_3N_4 and compared results obtained using empirical potentials and *ab initio* techniques based on DFT. We have then studied how the dielectric properties vary at the nanoscale. For both crystalline and amorphous samples we have adopted a model that takes into account the spatial variation of the dielectric response, at the microscopic scale, and we show that an abrupt interface model yields qualitatively incorrect results for the variation of the dielectric properties as a function of film thickness. We note that the electronic structures of crystalline Si_3N_4 slabs have been investigated using theoretical methods in Ref. 24 and Ref. 25. In addition, recently there have been extensive studies of crystalline β-Si_3N_4 thin films on Si, using either experimental[26] or theoretical techniques.[27,28] However investigations of dielectric properties have been extremely limited. Dielectric properties of amorphous thin film Si_3N_4 have been studied in experiment,[29–32] and recently we have provided a theoretical analysis based on DFT.[33] Here we build on our previous work and analyze in detail the relationship between the structural and electronic properties of amorphous films and their dielectric properties, and we compare an abrupt-interface semiclassical model with a microscopic model of dielectric constants.

The rest of the paper is organized as follows. In Sec. II we briefly review the methods used to calculate dielectric constants in the framework of DFT. Sections III, IV, and V discuss the dielectric properties of bulk crystalline, bulk amorphous, and thin film Si_3N_4, respectively. The summary and conclusions of the paper are presented in Sec. VI.

II. THEORETICAL METHOD

In this section, we describe how the dielectric constant is computed in extended systems using both density functional perturbation theory and a finite electric field approach based on the Berry phase formalism. In addition, we summarize the concept and calculation of the local dielectric constant, used in the case of surfaces and interfaces.

A. Extended systems

1. Density functional perturbation theory

The dielectric constant of an extended solid may be evaluated in the framework of density functional perturbation theory (DFPT) as described in Refs. 34 and 35. The static dielectric constant ϵ_0 includes an electronic contribution (ϵ_∞) and an ionic contribution:[35]

$$\epsilon_0^{\alpha\beta} = \epsilon_\infty^{\alpha\beta} + \frac{4\pi}{\Omega}\sum_m \frac{S_{m,\alpha\beta}}{\omega_m^2}. \quad (1)$$

Here Ω is the volume of the unit cell, ω_m denotes phonon mode frequencies, and $S_{m,\alpha\beta}$ are defined in terms of Born effective charges Z^*, atomic masses M, and normalized eigenmodes $u_{m,s}^{\alpha}$ of ion s along the direction α for a given mode m, which are obtained by diagonalizing the dynamical matrix:

$$S_{m,\alpha\beta} = \left(\sum_{s,\alpha'} Z_s^{*\alpha\alpha'} \frac{u_{m,s}^{\alpha'}}{\sqrt{M_s}}\right)\left(\sum_{s',\beta'} Z_{s'}^{*\beta\beta'} \frac{u_{m,s'}^{\beta'}}{\sqrt{M_{s'}}}\right). \quad (2)$$

Therefore, in this approach, in order to evaluate ϵ_0, one needs to calculate the dynamical matrix, which may be computationally demanding for large systems.

2. Finite electric field: Berry phase approach

An alternative approach to calculate the dielectric constant is to use the finite electric field method (FEF) coupled to a Berry phase formalism,[36–38] as described in Ref. 39. In this approach, an electric enthalpy functional is introduced:[39,40]

$$E^{\mathcal{E}} = E_{KS} - \Omega\mathcal{E}\cdot\mathbf{P}, \quad (3)$$

where E_{KS} is the Kohn-Sham total energy, $\mathcal{E}$ is a finite external electric field, and $\mathbf{P} = \mathbf{P}_{ion} + \mathbf{P}_{el}$ is the macroscopic polarization. In Ref. 39, the polarization is computed by minimizing the electric enthalpy functional using damping molecular dynamics techniques.[41] The system Brillouin zone (BZ) is sampled with a single k point, e.g., the Γ point, and the electronic polarization $\mathbf{P}_{el}$ is written using a Berry phase formalism:[37,38]

$$\mathbf{P}_{el} = -\frac{1}{\Omega}\frac{L}{\pi}\mathrm{Im}(\ln\det S[\{\psi_i\}])\mathbf{z}, \quad (4)$$

where $\mathbf{z}$ is the unit vector that indicates the direction of the applied electric field, $S[\{\psi_i\}]$ is a matrix defined in term of doubly occupied wave functions $\{\psi_i\}$: $S_{ij} = \langle\psi_i|e^{2\pi i z/L}|\psi_j\rangle$; L is the length of the cell in the direction of the applied electric field. We emphasize that Eq. (4) holds only in the case of BZ sampling with the Γ point. Both the static and high-frequency dielectric constants can be calculated from differences of the polarization evaluated for different values of the electric field. The advantage of this method is that the dynamical matrix calculation is avoided. However, size effects due to the Γ-point sampling may be severe and need to be carefully checked.[39,42]

B. Surfaces and interfaces: theory of local dielectric constants

A first-principles theory of atomic-scale dielectric constants at insulator interfaces was first developed by Giustino and Pasquarello.[43] It has been successfully applied to several systems such as Si slabs,[43–46] Si/SiO_2,[43,47] and polypropylene/metal-oxide[48] interfaces. Recently, the theory of local dielectric constants has been extended to study the dielectric properties of metal-insulator interfaces.[49,50] In this approach[43] a finite electric field is applied and a formalism based on the Berry phase theory of polarization[36–38] is adopted. Then a position dependent local dielectric constant is evaluated from induced polarizations, which are obtained by the induced charge densities due to the presence of the electric field.

An alternative way to apply a finite electric field to study local dielectric constants is to use an electric field derived from a sawtooth potential.[44,51] Consider an interface oriented along the z direction; we define the dielectric constant across the interface as the ratio between the projection of the electric displacement field D along the z direction, and the screened field $E(z)$:

$$\epsilon(z) = \frac{D}{E(z)}. \quad (5)$$

The screened electric field $E(z)$ can be obtained from the gradient of the change in the planar-averaged potential due to the applied electric field:[44,51]

$$E(z) = -\frac{\partial\Delta\overline{V}(z)}{\partial z}, \quad (6)$$

where the planar-averaged potential is defined as

$$\overline{V}(z) = \frac{1}{L_x L_y}\int_{x,y} V(x,y,z)dx\,dy. \quad (7)$$

L_x, L_y are the dimensions of the plane perpendicular to the interface.

The present definition of local dielectric constant is equivalent to that obtained in Ref. 43 but instead of using induced charge densities, we use the induced electrostatic potential. If the ions are fixed to their equilibrium positions, Eq. (5) yields the optical dielectric constant $\epsilon_\infty(z)$. If the ions are relaxed in response to a finite electric field, an ionic contribution is included in the evaluation of the dielectric constant and Eq. (5) yields the value of $\epsilon_0(z)$.

In practice, we are interested in the average dielectric constant of a finite system, so we define the average dielectric constant ϵ_{slab} of a slab representing a thin film using the relation[43]

$$\frac{l_{\mathrm{slab}}}{\epsilon_{\infty(0),\mathrm{slab}}} = \frac{x_2 - x_1}{\epsilon_{\infty(0),\mathrm{slab}}} = \int_{x_1}^{x_2}\frac{dz}{\epsilon_{\infty(0)}(z)}, \quad (8)$$

where x_1, x_2 define the slab boundaries (which are taken at the outermost atomic positions in all of our calculations) and $l_{\mathrm{slab}} = x_2 - x_1$ is the thickness of the slab. Using this approach, one is not only able to describe the microscopic variation of the dielectric constant through a thin film, but one can also obtain

TABLE I. Computed phonon frequencies (cm^{-1}) compared with experimental results and previous calculations.

Mode	Experiment (Ref. 56)	Ref. 14	This work
Raman			
E_{2g}	186	181	176
A_g	210	200	196
E_{1g}	229	225	218
E_{2g}	451	444	435
A_g	456	456	453
E_{2g}	619	610	608
A_g	732	725	717
E_{1g}	865	859	854
E_{2g}	928	921	917
A_g	939	930	926
E_{2g}	1047	1067	1030
Infrared			
A_u	380	378	354
E_{1u}	447	424	414
E_{1u}	580	562	554
A_u	910	848	843
E_{1u}	985	886	882
E_{1u}	1040	1021	1017

a quantitative estimate of the average dielectric constant of slabs representing thin films.

In the next section we discuss our results for the dielectric properties of the bulk first, and then of thin films.

III. BULK CRYSTALLINE SILICON NITRIDE

Among the three phases of crystalline Si_3N_4 we focus on β-Si_3N_4 since it is the most stable phase at ambient conditions.[15] The hexagonal unit cell of β-Si_3N_4 contains 14 atoms, and it is described by six structural parameters[12] (a,c, and four internal parameters). We first optimized the structure of β-Si_3N_4 using DFT within the local density approximation (LDA), a $4 \times 4 \times 10$ k-point grid,[55] a plane wave basis with a kinetic energy cutoff of 80 Ry, in conjunction with norm-conserving pseudopotentials. We carried out calculations with the QUANTUM ESPRESSO code.[54] For structural properties, our results (7.570 Å, 2.892 Å, 0.173, 0.766, 0.330, 0.028) are in good agreement with experiment (7.607 Å, 2.911 Å, 0.174, 0.766, 0.321, 0.025)[12] and previous theoretical work (7.557 Å, 2.885 Å, 0.174, 0.768, 0.321, 0.030).[14] We also compared selected phonon frequencies with available measurements[56] and DFT calculations[14] and obtained a good agreement with existing data, as shown in Table I. In addition, the measured band gap of β-Si_3N_4 (4.6-5.5 eV)[57] is reproduced fairly well by the LDA (we obtain a value of 4.4 eV).

TABLE II. Dielectric constant [$\epsilon = \frac{1}{3}\mathrm{Tr}(\epsilon^{\alpha\beta})$ where $\epsilon^{\alpha\beta}$ are elements of the dielectric tensor] of β-Si_3N_4: Comparison between our results and those of previous DFT calculations (Ref. 58) and experiment (Ref. 67).

Dielectric constant	Experiment (Ref. 67)	DFT calculation (Ref. 58)	This work
ϵ_∞		4.33	4.23
ϵ_0	8.4–8.66	8.19	8.25

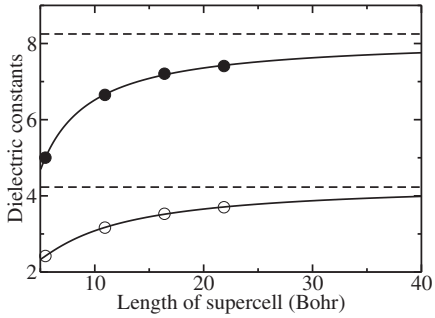

FIG. 1. Static (filled symbols) and optical (empty symbols) dielectric constant of β-Si_3N_4 as a function of the size of supercell adopted in the finite electric field calculations. Dashed lines are results obtained using density functional perturbation theory.

We have calculated optical and static dielectric constants of β-Si_3N_4 using DFPT. In Table II, we summarize the average value of the dielectric constant [$\epsilon = \frac{1}{3}\mathrm{Tr}(\epsilon)$] and compare with results from available experiments and previous theoretical work. Our results for ϵ_∞ and ϵ_0 agree very well with the DFT calculation of Ref. 58. In addition, our computed static dielectric constant ϵ_0 falls into the range of experimental data (8.4–8.66).[67]

One may also compute the dielectric constants of β-Si_3N_4 using the FEF method in conjunction with a Berry phase formalism.[39] However, size effects due to the use of Γ-point sampling in molecular dynamics calculations are severe. As an example, in Fig. 1 we show the dielectric constants of β-Si_3N_4 obtained with the FEF method as functions of the size of the simulation cell L. Convergence is obtained for large L ($L >$ 40 bohrs), and it is rather slow.[39,42,43]

IV. BULK AMORPHOUS SILICON NITRIDE

We have generated two amorphous structures of Si_3N_4. All the models were generated starting from a molten β-Si_3N_4 bulk sample at 3000 K, obtained using classical molecular dynamics (MD) with a modified Tersoff potential.[16] The bulk liquids were then slowly annealed to room temperature. Starting from classically annealed configurations, we then conducted *ab initio* MD simulations to refine our Si_3N_4 amorphous models. All samples underwent an additional annealing cycle by being heated up to 2000 K and quenched down to room temperature for about $2 \sim 3$ ps, using *ab initio* MD employing the QBOX code.[59] In all of our simulations, the density was fixed to the experimental value. To understand size effects on structural and dielectric properties of the amorphous Si_3N_4, we generated two models (I and II) containing 56 and 168 atoms, respectively, using the same protocol in both cases.

A. Structural properties

We first discuss the structural properties of our amorphous models. In Fig. 2 the dotted and solid lines represent the calculated pair correlation functions (PCFs) of model I and model II, respectively. The Si-N and N-N PCFs of our two

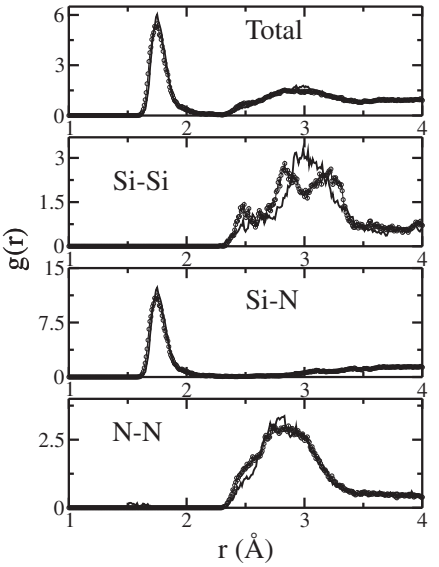

FIG. 2. Pair correlation functions $[g(r)]$ of two amorphous Si_3N_4 samples generated by *ab initio* MD: Model I with 56 atoms (dotted line) and model II with 168 atoms (solid line).

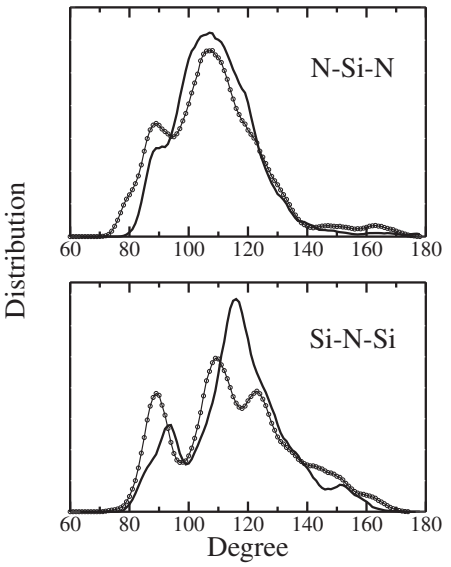

FIG. 3. Angle distribution function of amorphous Si_3N_4 samples generated using *ab initio* MD: Model I with 56 atoms (dotted line) and model II with 168 atoms (solid line).

amorphous models are very similar. The main peaks in Si-N and N-N PCFs are located at 1.74 Å and 2.83 Å, and they are related to the first and second peak at 1.73 Å and 2.81 Å in the radial distribution function detected experimentally.[60] Size effects can be seen by comparing the Si-Si PCFs obtained for the two models: The large sample (model II) exhibits only one peak in the Si-Si PCF, while the smaller one (model I) has several peaks.

The angle distributions for our models are shown in Fig. 3; the distribution of N-Si-N angles has a main peak located at around 110 ° which is very close to the ideal tetrahedral angle of 109.47°, indicating the presence of SiN_4 tetrahedral units. In addition, our model shows quasiplanar NSi_3 units, as the main peak in the Si-N-Si angle distribution is at 117°, consistent with the value of 120° for regular planar NSi_3 units. Size effects are also shown in the Si-N-Si angle distribution, which has a much more pronounced peak at small angles in model II.

We note that angle distributions of samples generated classically show significant differences from those obtained from *ab initio* calculations. As shown in Fig. 3, in addition to the main peak, the Si-N-Si and N-Si-N angle distributions derived *ab initio* also exhibit a distinct peak at about 90°, in agreement with a recent first-principles work on a-Si_3N_4.[23] However, such configurations could not be obtained in models generated by classical potentials.[16–19]

To compare with experiment, we have calculated the neutron structure factor[61] of the larger sample with 168 atoms. We used neutron scattering lengths of 4.15 fm and 9.36 fm for Si and N, respectively.[62] As seen in Fig. 4, overall the agreement with experiment is very good. We note that our results also agree well with those of a recent *ab initio* calculation for a model with 152 atoms.[23]

In Fig. 5 we show the electronic density of states (DOS) of the model with 168 atoms calculated at the LDA level and we find a band gap of 2.1 eV, an underestimate of the experimental value of 4.5–5.3 eV.[63,64]

B. Dielectric constant

We have calculated the dielectric constants of the two models of a-Si_3N_4 using DFPT. The dielectric tensors of model I are

$$\epsilon_\infty = \begin{pmatrix} 4.65 & -0.08 & 0.03 \\ -0.08 & 4.83 & -0.01 \\ 0.03 & -0.01 & 4.95 \end{pmatrix},$$

$$\epsilon_0 = \begin{pmatrix} 11.88 & 0.58 & 0.14 \\ 0.58 & 11.05 & 0.13 \\ 0.14 & 0.13 & 10.86 \end{pmatrix},$$

with an average value of 4.81 for the optical dielectric constant and 11.26 for the static dielectric constant. The dielectric tensors of model II are

$$\epsilon_\infty = \begin{pmatrix} 5.18 & -0.02 & 0.10 \\ -0.02 & 5.03 & 0.01 \\ 0.10 & 0.01 & 5.09 \end{pmatrix},$$

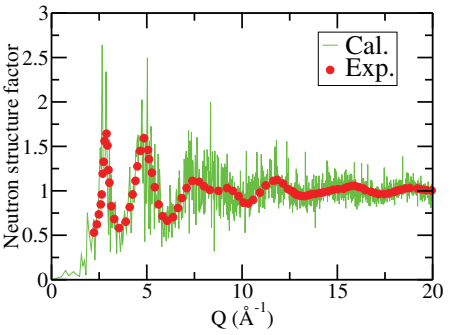

FIG. 4. (Color online) Neutron scattering structure factor of amorphous Si_3N_4 calculated for model II (see Fig. 3) at room temperature (solid line), compared to the experimental data (circle symbols) (Ref. 60).

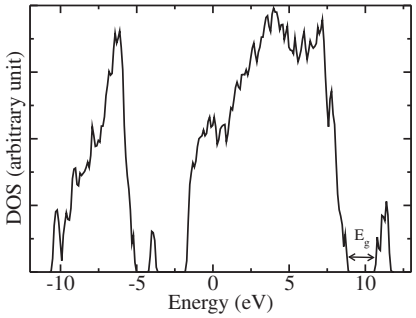

FIG. 5. Electronic density of states of amorphous Si_3N_4 calculated for model II.

$$\epsilon_0 = \begin{pmatrix} 11.40 & 0.13 & 0.50 \\ 0.13 & 11.23 & 0.00 \\ 0.50 & 0.00 & 11.31 \end{pmatrix},$$

corresponding to an average value of 5.1 for the optical dielectric constant and 11.31 for the static dielectric constant. In both cases, we obtain nearly diagonal and isotropic dielectric tensors. Our results indicate that dielectric constants are weakly affected by the size of the amorphous sample.

The dielectric constants obtained for the two bulk amorphous samples are higher than those reported recently[23] using a FEF technique. The differences are $\Delta\epsilon_0 = 2.46$ (2.51) and $\Delta\epsilon_\infty = 0.91$ (1.2) for model I (II) and may be due to convergence issues of the FEF method using a Berry phase formalism, similar to what we found in the case of crystalline Si_3N_4 (see Fig. 1). Direct comparison of calculated dielectric constants of bulk amorphous Si_3N_4 with experiment is difficult because of two reasons: (i) The experimental measurements of dielectric constants are usually performed with amorphous thin films; (ii) the sample preparation procedure may vary and result in amorphous samples with different structural properties. The values of static dielectric constants of amorphous Si_3N_4 reported in the literature vary between 7.0 and 11.0,[65–69] depending on the preparation condition. Therefore our computed values are in reasonable agreement with experiments, given these uncertainties.

V. SILICON NITRIDE SLABS

In this section we first describe the crystalline and amorphous Si_3N_4 slab models used in our calculation. We introduce and apply a classical model for the case of crystalline Si_3N_4 slabs and we then show the need for a description of the dielectric constant at the microscopic level. Finally, we present microscopic descriptions of dielectric constants for both crystalline and amorphous Si_3N_4 slabs.

A. Structural models

To understand the effect of the size reduction on the dielectric properties of Si_3N_4, we have built crystalline slabs with different thicknesses and different growth directions. We investigated two growth directions, the [0001] direction by using a hexagonal unit cell,[24] and the [010] direction using an orthorhombic unit cell.[70] We terminated the surface dangling bonds on each side of the slabs by hydrogen atoms, and we optimized the ionic positions of the whole slab. To avoid the interaction between slabs in neighboring supercells, we have used a vacuum region 15 Å thick in our calculations.

In order to understand the difference in dielectric properties between crystalline and amorphous Si_3N_4 thin films, we generated several amorphous slab models by combining classical and *ab initio* MD simulations. A Si_3N_4 crystalline cell was first melted at 3000 K by using a modified Tersoff potential.[16] About 10 Å vacuum was added along the z axis to the bulk liquid in order to generate two free surfaces. Using this structure as the starting configuration, we conducted a classical MD simulation at 3000 K and collected seven snapshots along the MD trajectory every 100 ps. This ensures that the generated snapshots are structurally uncorrelated. Each of the seven snapshots was then equilibrated at 2000 K and annealed to room temperature for about 2 ps using *ab initio* MD employing the QBOX code.[59] Finally, all atoms of the annealed configurations were fully relaxed to their positions of the nearest energy minimum. At variance with crystalline slabs, the surfaces of our amorphous thin films were not hydrogen terminated.

B. Dielectric constant

1. Abrupt interface model

We first address the question of how to use DFPT and FEF methods to calculate the dielectric constant of finite systems such as Si_3N_4 thin films. The dielectric constant obtained from supercell calculations is not the dielectric constant of an isolated slab but rather that of a system consisting of the slab plus the vacuum regions.[71,72] Therefore, in principle the dielectric constant obtained with supercell calculations depends on the thickness of the vacuum regions, and in order to apply directly DFPT or FEF techniques, one needs to introduce a model to extract the dielectric constant of the slab.

One model used in the literature[73,74] is the so-called abrupt interface model, where one assumes that the dielectric constant attains an average value ϵ_{slab} that is constant throughout the slab. At the surface, one assumes that the dielectric constant decreases sharply from ϵ_{slab} to the dielectric constant of vacuum ($\epsilon = 1.0$). Therefore in this model all the spatial variations of the dielectric constant inside the slab are neglected, as well as variations at the interface between the slab and vacuum. Within these assumptions, one can derive a relation between the dielectric constant of the slab and that of the supercell, based on classical electrostatics:

$$\left(\frac{1}{\epsilon_{\infty(0),sc}} - 1\right)L = \left(\frac{1}{\epsilon_{\infty(0),\text{slab}}} - 1\right)l_{\text{slab}}. \tag{9}$$

In Eq. (9), L and l_{slab} are the thickness of the supercell and that of the isolated slab, respectively. The dielectric constant $\epsilon_{\infty(0),\text{slab}}$ and $\epsilon_{\infty(0),sc}$ are the optical (static) dielectric constants of the slab and the supercell, respectively. In our calculations the thickness of the slab is computed from the positions of the outermost hydrogen atoms. We note that in this model, the quantity that needs to be converged with respect to the extension of vacuum in the supercell is the product $(\frac{1}{\epsilon_{\infty(0),sc}} - 1)L$. Once convergence is ensured,[75] one may extract the dielectric constant of the slab $\epsilon_{\infty,\text{slab}}$ ($\epsilon_{0,\text{slab}}$) from $\epsilon_{\infty,sc}$ ($\epsilon_{0,sc}$).

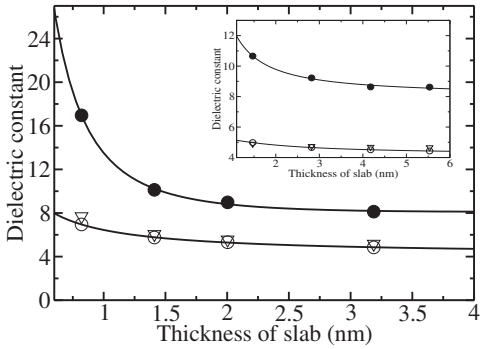

FIG. 6. Dielectric constant ϵ_{slab} as function of the thickness of slabs grown in the [0001] and [010] (inset) directions, computed using an abrupt interface model. Circles (triangles) represent the results from FEF (DFPT) calculations. Open (filled) symbols represent $\epsilon_{\infty,\text{slab}}$ ($\epsilon_{0,\text{slab}}$).

In principle, $\epsilon_{0,sc}$ could be obtained from DFPT calculations by adding the ionic contribution to $\epsilon_{\infty,sc}$. However the calculation of dynamical matrices and phonon vibrational modes are very demanding for systems with several tens of atoms. To overcome this problem, we used the FEF method[39] to obtain $\epsilon_{0,sc}$. Since a very large supercell was used in our calculations, the size effects due to Γ-point sampling are not of concern here. As an additional check, we compared the results for $\epsilon_{\infty,sc}$ obtained with FEF and DFPT calculations and found a very good agreement, as seen in Fig. 6.

In Fig. 6 we present the computed dielectric constant ϵ_{slab} as a function of thickness as obtained from Eq. (9). The results show that both the static and high-frequency dielectric constant of Si_3N_4 slabs significantly increase with decreasing thickness. For the thinnest slab, the dielectric constants of the slab are almost twice as large as those of bulk Si_3N_4. For increasing thicknesses, the dielectric constants decay to the bulk value. To understand how the surface and the growth direction may affect the value of the dielectric constant, we considered different growth directions. Following Ref. 70 we built an orthorhombic supercell with 28 atoms, then slabs with different thicknesses (consisting of one to four primitive unit cells) were

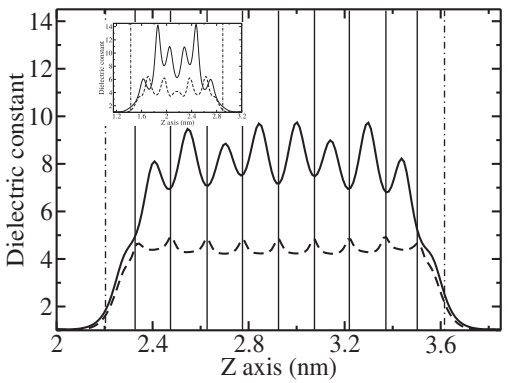

FIG. 7. Spatial variation of the optical (dashed line) and static (solid line) dielectric constants along the z direction (parallel to the growth direction) for crystalline Si_3N_4 slabs grown in the [0001] and [010] (inset) directions. Vertical lines represent planes of Si_3N_4 (solid) and the positions of the outermost H atoms (dash-dotted line).

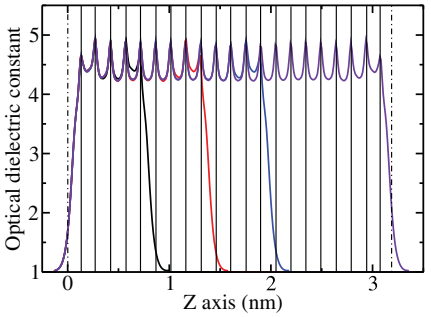

FIG. 8. (Color online) Spatial variation of the optical dielectric constants along the z direction (parallel to the growth direction) for crystalline Si_3N_4 slabs grown in the [0001] direction. Vertical lines represent planes of Si_3N_4 (solid) and the positions of the outermost H atoms (dash-dotted line). The value of the bulk dielectric constant ϵ_∞ is 4.23.

generated by cutting the crystal in the [010] direction. In the inset of Fig. 6 we present ϵ_{slab} as a function of thickness for orthorhombic slabs. The high-frequency dielectric constant $\epsilon_{\infty,\text{slab}}$ again shows good agreement between DFPT and FEF calculations. Furthermore, both static and high-frequency dielectric constants significantly increase with decreasing slab thickness. Therefore, it is reasonable to expect that within the abrupt interface model the dielectric constant of Si_3N_4 always increases as the slab thickness decreases, irrespective of the growth direction.

These results are not consistent with experimental data showing that the dielectric constant of Si_3N_4 thin films is smaller than that of the bulk.[29–32] We now turn to a more refined model taking into account microscopic variations of the dielectric constant.

2. *Microscopic description of dielectric constant*

We computed the dielectric constant of a slab as a function of z, i.e., the growth direction, by applying a sawtooth potential as described in Sec. II. Since we carried out calculations with periodic boundary conditions, an artificial planar dipole potential was added to our simulation cell, following the prescription proposed in Refs. 52 and 53. When ionic relaxations are allowed, $\Delta\overline{V}(z)$ has an oscillatory behavior that can be smoothed out by using Gaussian convolution techniques with

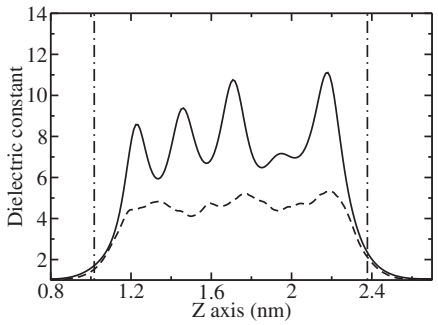

FIG. 9. Spatial variation of the optical (dashed line) and static (solid line) dielectric constants along the z direction (perpendicular to the slab surfaces) of an amorphous slab. Vertical lines represent the positions of the outermost H atoms.

a choice of standard deviation σ.[76] This is equivalent to the assumption that the dielectric response of the system is local over a scale of σ.[43]

Figure 7 shows $\epsilon(z)$ for a crystalline slab grown in the [0001] direction. Consistent with previous studies on silicon slabs,[43–46] we find that the dielectric constant decays smoothly at the surface. The periodic oscillations of the dielectric constant within the slab originates from the ordered structure of the crystalline thin film. We also show $\epsilon(z)$ for crystalline slab grown in the [010] direction in the inset of Fig. 7. The difference in the dielectric constant profile is due to the difference of the atomic arrangement in the two films grown in different directions. We note that for a given slab configuration, the average value of the dielectric screening inside the slab is basically constant as a function of size (see Fig. 8 for $\epsilon_\infty(z)$ computed for crystalline Si_3N_4 slabs with different thicknesses grown in the [0001] direction) and that the decay at the surface occurs within 2 atomic layers in all cases.

In Fig. 9 we show the spatial variation of the dielectric constant along the z axis of one model of an amorphous silicon nitride slab. As expected, the dielectric constant shows a nonhomogeneous behavior within the slab, due to the disordered arrangement of atoms.

We have evaluated the average dielectric constant using Eq. (8). In Fig. 10 the results for various crystalline slabs of different thicknesses grown in the [0001] and [010] directions are represented by circle and square symbols, respectively. At variance from results obtained with the abrupt interface model (Fig. 6), crystalline slabs show a substantially reduced screening with respect to the bulk value below 4 nm (the bulk value is indicated by dashed lines in Fig. 6). This reduction is due to the decay of the dielectric constant in proximity to the surface and it depends on the film growth direction. As the thickness of the slab becomes smaller, the ratio of surface to volume increases, inducing a stronger reduction in the dielectric constant. It is interesting to note that for both growth directions, while the optical dielectric constant reaches values close to that of the bulk already for thicknesses of about 5 nm, $\epsilon_{0,\mathrm{slab}}$ remains smaller than that of the bulk for thicknesses up to 10 nm. In addition,

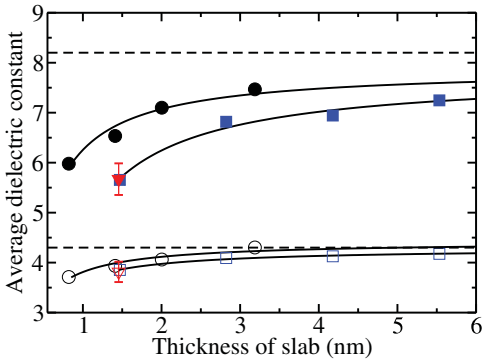

FIG. 10. (Color online) Dielectric constant of crystalline slabs grown in the [0001] (circles) and [010] (squares) direction compared to that of amorphous slabs (triangles). Open (filled) symbols represent $\epsilon_{\infty,\mathrm{slab}}$ ($\epsilon_{0,\mathrm{slab}}$). Dashed lines indicate values of the dielectric constants for bulk crystalline Si_3N_4.

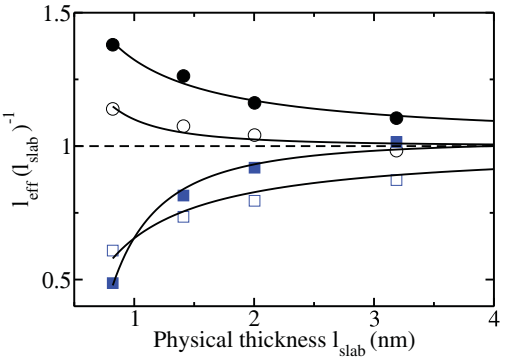

FIG. 11. (Color online) The ratio $l_{\mathrm{eff}}(l_{\mathrm{slab}})^{-1}$ as a function of the physical slab thickness l_{slab} for crystalline slabs grown in the [0001] direction (see text). Open (filled) circles and squares symbols represent the results with $\epsilon_{\mathrm{slab}} = \epsilon_{\infty,\mathrm{slab}}$ ($\epsilon_{\mathrm{slab}} = \epsilon_{0,\mathrm{slab}}$) obtained from Eq. (8) and Eq. (9), respectively.

we find that at the nanoscale, the static dielectric constant is much more sensitive to the growth direction, as indicated in Fig. 10.

An alternative way to display our data for the slab dielectric properties comes from the use of the concept of "effective dielectric thickness" l_{eff}, which is defined as follows:

$$\frac{l_{\mathrm{slab}}}{\epsilon_{\mathrm{slab}}} = \frac{l_{\mathrm{eff}}}{\epsilon_{\mathrm{bulk}}}. \tag{10}$$

Here l_{slab} is the physical slab thickness, as obtained from the positions of the outermost atoms of the slab; ϵ_{slab} and ϵ_{bulk} are the dielectric constants of the slab and of bulk crystalline Si_3N_4, respectively. We consider two cases: One where the dielectric constant $\epsilon_{\mathrm{slab}} = \epsilon_{\infty(0),\mathrm{slab}}$ is obtained with the abrupt interface model [using Eq. (9)], and the second one where the dielectric constant is obtained from a microscopic description [using Eq. (8)]. The effective dielectric thickness l_{eff} is the slab thickness at which the dielectric properties of bulk Si_3N_4 are recovered.

In Fig. 11 and Fig. 12 we show how the ratio $l_{\mathrm{eff}}(l_{\mathrm{slab}})^{-1}$ varies as a function of the physical slab thickness l_{slab} for crystalline slabs grown in the [0001] and [010] directions,

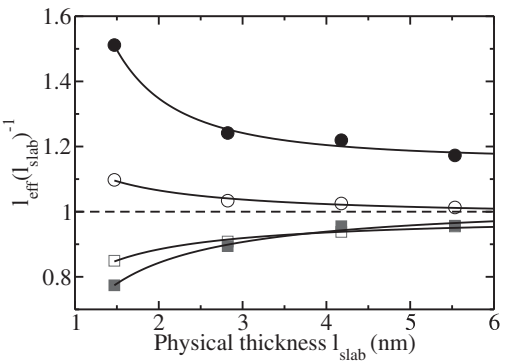

FIG. 12. The ratio $l_{\mathrm{eff}}(l_{\mathrm{slab}})^{-1}$ as a function of the physical slab thickness l_{slab} for crystalline slabs grown in the [010] direction. Open (filled) circles and squares symbols represent the results with $\epsilon_{\mathrm{slab}} = \epsilon_{\infty,\mathrm{slab}}$ ($\epsilon_{\mathrm{slab}} = \epsilon_{0,\mathrm{slab}}$) obtained from Eq. (8) and Eq. (9), respectively.

respectively, with $\epsilon_{slab} = \epsilon_{\infty,slab}$ ($\epsilon_{0,slab}$) obtained using either Eq. (8) or Eq. (9). For both growth directions, within the abrupt interface model, $l_{eff}(l_{slab})^{-1}$ decreases with decreasing physical slab thickness l_{slab} and reaches 1.0 at large l_{slab}. Therefore at the nanoscale, within the abrupt interface model, l_{eff}, the thickness at which the bulk dielectric properties are recovered, is even smaller than the physical thickness of the slab, clearly indicating an unphysical description provided by the model. On the contrary, using the microscopic description of dielectric constants, $l_{eff}(l_{slab})^{-1}$ increases with decreasing physical thickness of the slabs, reproducing a correct behavior of dielectric properties as a function of size. While the two models provide identical results at large physical slab thickness, by neglecting the variations of dielectric constants at the interfaces, the abrupt interface model leads to a incorrect behavior of dielectric properties at the nanoscale ($l_{slab} <$ 6 nm). We note that the behavior of the dielectric screening as a function of thickness found here using a fully microscopic model (Fig. 10) is similar to the one reported for Si slabs.[43] The results of Ref. 43 have been recently confirmed by experiment.[77,78]

Finally we studied the average dielectric constants of amorphous slabs using a microscopic description. In Fig. 10 the triangular symbols represent the dielectric constant of amorphous models that have the same thickness as that of a nine-layer crystalline [0001] slab. We first calculated the dielectric constants for seven different amorphous slab models, then the mean value and standard deviations of dielectric constants were obtained. We note that both optical and static dielectric constants are very similar for the several amorphous slab models considered here, with deviations $\sigma_{\epsilon_\infty} = 0.2$ and $\sigma_{\epsilon_0} = 0.31$, respectively. Both the static and optical dielectric response of the amorphous slabs are smaller than that of the crystalline [0001] slab with the same thickness. However they are of the same order as that of the orthorhombic slab. This indicates that amorphization of thin films may be an important factor in decreasing the dielectric constant at the nanoscale. All of our results show that the presence of a surface in the film greatly affects its average dielectric properties and indicates that surface and interface effects play a key role in determining the dielectric response at the nanoscale. It is interesting to note that for both amorphous and crystalline Si_3N_4 slabs with thicknesses of about 1 nm, the dielectric constant is still larger that of SiO_2 ($\epsilon_0 = 4.6$, $\epsilon_\infty = 2.46$).[58]

VI. CONCLUSION

In conclusion, we have investigated the dielectric properties of bulk and thin film silicon nitride by using first-principles density functional theory calculations. We have calculated the dielectric constant of bulk crystalline and bulk amorphous Si_3N_4 by employing both density functional perturbation theory and finite electric field techniques. For crystalline Si_3N_4, our results ($\epsilon_0 = 8.25, \epsilon_\infty = 4.23$) agree well with experiment and other theoretical work. By considering several model structures for bulk amorphous Si_3N_4, generated by *ab initio* molecular dynamics, we investigated the dependence of structural and dielectric properties on the size of the simulated system. Samples with at least $\simeq$150 atoms are necessary to accurately describe the structural properties of a-Si_3N_4. For example, using a system with 168 atoms, we find very good agreement between computed and measured neutron structure factors. In addition we found important qualitative differences between samples generated using classical MD and *ab initio* calculations. The computed static and optical dielectric constants of our amorphous models are higher than those obtained for the crystalline phase and consistent with available experimental data.

We also investigated the dielectric properties of crystalline and amorphous silicon nitride thin films with thickness below 10 nm. By using an abrupt interface model, we showed the need to take into account the microscopic variation of dielectric constants at the surface of the films, in order to reproduce the correct behavior of dielectric properties as a function of size. We then calculated the dielectric constant of silicon nitride films as a function of thickness using a detailed microscopic model. For crystalline films we find nonnegligible variations of the static dielectric constants with respect to bulk values for thicknesses up to 10 nm and a reduction as large as factors of 1.32 and 1.15 for, e.g., 1 and 2 nm slabs grown in the [0001] direction, respectively. Amorphization, that is, atomic disorder, may further decrease both the high-frequency and the static dielectric constants of the films. Work is in progress to study the dependence of dielectric properties of silicon nitride thin films on surface and interface geometries.

ACKNOWLEDGMENTS

We acknowledge financial support from Intel and the use of Teragrid computational resources. We are grateful for useful discussions with S. Hamel and D. Donadio.

[1] F. L. Riley, J. Am. Ceram. Soc. **83**, 245 (2000).
[2] M. H. Bocanegra-Bernal and B. Matovic, Mater. Sci. Eng. A **527**, 1314 (2010).
[3] J. Schmidt, M. J. Kerr, and A. Cuevas, Semicond. Sci. Technol. **16**, 164 (2001).
[4] B. Sopori, J. Electron. Mater. **32**, 1034 (2003).
[5] I. Fernandez-Cuesta, X. Borrise, and F. Perez-Murano, Nanotechnology **16**, 2731 (2005).
[6] I. Fernandez-Cuesta, X. Borrise, and F. Perez-Murano, J. Vac. Sci. Technol. B **24**, 2988 (2006).
[7] M. J. Powell, B. C. Easton, and O. F. Hill, Appl. Phys. Lett. **38**, 10 (1981).
[8] G. D. Wilk, R. M. Wallace, and J. M. Anthony, J. Appl. Phys. **89**, 5243 (2001).
[9] T. P. Ma, IEEE Trans. Electron Devices **45**, 680 (1998).
[10] Y. C. Yeo, Q. Lu, W. C. Lee, T. J. King, C. M. Hu, X. M. Wang, X. Guo, and T. P. Ma, IEEE Electron Device Lett. **21**, 540 (2000).
[11] Y. C. Yeo, T. J. King, and C. M. Hu, Appl. Phys. Lett. **81**, 2091 (2002).
[12] R. W. G. Wyckoff, *Crystal Structures*, Vol. 2 (John Wiley and Sons, New York, 1963).
[13] A. Y. Liu and Marvin L. Cohen, Phys. Rev. B **41**, 10727 (1990).
[14] Y. Cai, L. Zhang, Q. Zeng, L. Cheng, and Y. Xu, Phys. Rev. B **74**, 174301 (2006).

[15] A. Kuwabara, K. Matsunaga, and I. Tanaka, Phys. Rev. B **78**, 064104 (2008).

[16] F. de Brito Mota, J. F. Justo, and A. Fazzio, Phys. Rev. B **58**, 8323 (1998).

[17] L. Ouyang and W. Y. Ching, Phys. Rev. B **54**, R15594 (1996).

[18] S. R. Billeter, A. Curioni, D. Fischer, and W. Andreoni, Phys. Rev. B **73**, 155329 (2006).

[19] P. Vashishta, R. K. Kalia, and I. Ebbsjo, Phys. Rev. Lett. **75**, 858 (1995).

[20] F. Alvarez, C. C. Diaz, A. A. Valladares, and R. M. Valladares, Phys. Rev. B **65**, 113108 (2002).

[21] F. Alvarez and A. A. Valladares, Phys. Rev. B **68**, 205203 (2003).

[22] J. F. Justo, F. de Brito Mota, and A. Fazzio, Phys. Rev. B **65**, 073202 (2002).

[23] L. Giacomazzi and P. Umari, Phys. Rev. B **80**, 144201 (2009).

[24] V. M. Bermudez, Surf. Sci. **579**, 11 (2005).

[25] J. C. Idrobo, H. Iddir, S. Ogut, A. Ziegler, N. D. Browning, and R. O. Ritchie, Phys. Rev. B **72**, R241301 (2005).

[26] X. S. Wang, G. Zhai, J. Yang, and N. Cue, Phys. Rev. B **60**, R2146 (1999).

[27] G. L. Zhao and M. E. Bachlechner, Phys. Rev. B **58**, 1887 (1998).

[28] M. Yang, R. Q. Wu, W. S. Deng, L. Shen, Z. D. Sha, Y. Q. Cai, Y. P. Feng, and S. J. Wang, J. Appl. Phys. **105**, 024108 (2009).

[29] S. M. Hu, J. Electrochem. Soc. **113**, 693 (1966).

[30] E. A. Taft, J. Electrochem. Soc. **118**, 1341 (1971).

[31] Z. Wang, M. A. Kelly, Z. Shen, G. Wang, X. Xiang, and J. T. Wetzel, J. Appl. Phys. **92**, 808 (2002).

[32] A. Karbassi, D. Ruf, A. D. Bettermann, C. A. Paulson, D. W. van der Weide, H. Tanbakuchi, and R. Stancliff, Rev. Sci. Instrum. **79**, 094706 (2008).

[33] T. A. Pham, T. Li, S. Shankar, F. Gygi, and G. Galli, Appl. Phys. Lett. **96**, 062902 (2010).

[34] S. Baroni, S. de Gironcoli, A. D. Corso, and P. Giannozzi, Rev. Mod. Phys. **73**, 515 (2001).

[35] X. Gonze and C. Lee, Phys. Rev. B **55**, 10355 (1997).

[36] R. D. King-Smith and D. Vanderbilt, Phys. Rev. B **47**, 1651 (1993).

[37] R. Resta, Rev. Mod. Phys. **66**, 899 (1994).

[38] R. Resta, Phys. Rev. Lett. **80**, 1800 (1998).

[39] P. Umari and A. Pasquarello, Phys. Rev. Lett. **89**, 157602 (2002).

[40] I. Souza, J. Íñiguez, and D. Vanderbilt, Phys. Rev. Lett. **89**, 117602 (2002).

[41] R. Car and M. Parrinello, Phys. Rev. Lett. **55**, 2471 (1985).

[42] P. Umari and A. Pasquarello, Phys. Rev. B **68**, 085114 (2003).

[43] F. Giustino and A. Pasquarello, Phys. Rev. B **71**, 144104 (2005).

[44] S. Hamel, A. J. Williamson, H. F. Wilson, F. Gygi, G. Galli, E. Ratner, and D. Wack, Appl. Phys. Lett. **92**, 043115 (2008).

[45] J. Nakamura, S. Ishihara, A. Natori, T. Shimizu, and K. Natori, J. Appl. Phys. **99**, 054309 (2006).

[46] J. Nakamura and K. Natori, Appl. Phys. Lett. **89**, 053118 (2006).

[47] N. Shi and R. Ramprasad, Phys. Rev. B **74**, 045318 (2006).

[48] L. Yu, V. Ranjan, M. B. Nardelli, and J. Bernholc, Phys. Rev. B **80**, 165432 (2009).

[49] M. Stengel and N. A. Spaldin, Phys. Rev. B **75**, 205121 (2007).

[50] M. Stengel, D. Vanderbilt, and N. A. Spaldin, Nature Mater. **8**, 392 (2009).

[51] R. Resta and K. Kunc, Phys. Rev. B **34**, 7146 (1986).

[52] B. Meyer and D. Vanderbilt, Phys. Rev. B **63**, 205426 (2001).

[53] L. Bengtsson, Phys. Rev. B **59**, 12301 (1999).

[54] P. Giannozzi, S. Baroni, N. Bonini, M. Calandra, R. Car, C. Cavazzoni, D. Ceresoli, G. L. Chiarotti, M. Cococcioni, I. Dabo, A. Dal Corso, S. de Gironcoli, S. Fabris, G. Fratesi, R. Gebauer, U. Gerstmann, C. Gougoussis, A. Kokalj, M. Lazzeri, L. Martin-Samos, N. Marzari, F. Mauri, R. Mazzarello, S. Paolini, A. Pasquarello, L. Paulatto, C. Sbraccia, S. Scandolo, G. Sclauzero, A. P. Seitsonen, A. Smogunov, P. Umari, and R. M. Wentzcovitch, J. Phys. Condens. Matter **21**, 395502 (2009); [http://www.quantum-espresso.org].

[55] H. J. Monkhorst and J. D. Pack, Phys. Rev. B **13**, 5188 (1976).

[56] N. Wada, S. A. Solin, J. Wong, and S. Prochazka, J. Non-Cryst. Solids **43**, 7 (1981).

[57] R. D. Carson and S. E. Schnatterly, Phys. Rev. B **33**, 2432 (1986) and references therein.

[58] D. Fischer, A. Curioni, S. Billeter, and W. Andreoni, Phys. Rev. Lett. **92**, 236405 (2004).

[59] F. Gygi, QBOX, a scalable implementation of first-principles molecular dynamics [http://eslab.ucdavis.edu].

[60] M. Misawa, T. Fukunaga, K. Niihara, T. Hirai, and K. Suzuki, J. Non-Cryst. Solids **34**, 313 (1979).

[61] Yoshio Waseda, *The Structure of Non-Crystalline Materials: Liquids and Amorphous Solids* (McGraw-Hill, New York, 1980).

[62] See [http://www.ncnr.nist.gov/resources/n-lengths/].

[63] G. E. Jellison and F. A. Modine, Appl. Phys. Lett. **69**, 371 (1996).

[64] J. Bauer, Phys. Status Solidi A **39**, 411 (1977).

[65] J. S. Thorp and R. I. Sharif, J. Mater. Sci. **12**, 2274 (1977).

[66] J. S. Thorp, A. B. Ahmad, B. L. J. Kulesza, and T. G. Bushell, J. Mater. Sci. **19**, 3680 (1984).

[67] T. Goto and T. Hirai, J. Mater. Sci. **24**, 821 (1989) and references therein.

[68] G. Rieder and F. Olcaytug, Thin Solid Films **89**, 95 (1982).

[69] C. E. Morosanu, Thin Solid Films **65**, 171 (1980).

[70] S. Ogata, N. Hirosaki, C. Kocer, and H. Kitagawa, Phys. Rev. B **64**, 172102 (2001).

[71] E. K. Yu, D. A. Stewart, and S. Tiwari, Phys. Rev. B **77**, 195406 (2008).

[72] J. Tobik and A. D. Corso, J. Chem. Phys. **120**, 9934 (2004).

[73] N. Shi and R. Ramprasad, Phys. Rev. B **75**, 155429 (2007).

[74] T. Ono and K. Hirose, Phys. Rev. B **72**, 085105 (2005).

[75] For example, for a 5-layer Si_3N_4 slab grown in the [0001] direction we obtain the following values of $\epsilon_{\infty,\mathrm{slab}}$ as a function of L: 7.68,7.69,7.69 for $L = 71.0, L = 109.0, L = 164.0$ (bohrs), respectively.

[76] In all our calculations the value of the standard deviation σ is set to 0.6–0.8 Å, which is about half the distance between neighboring atomic layers of crystalline Si_3N_4. This choice of the standard deviation is sufficient to remove the oscillatory behavior of $\Delta\overline{V}(z)$ and typically leads to an error of $\Delta \approx 0.3$ in dielectric constant calculations for the systems studied here within the chosen range of σ.

[77] H. G. Yoo and P. M. Fauchet, Phys. Rev. B **77**, 115355 (2008).

[78] H. G. Yoo and P. M. Fauchet, Phys. Rev. B **77**, 209903(E) (2008).